Microsc. Microanal. 18, 1342–1354, 2012
doi:10.1017/S1431927612013335

Microscopy AND Microanalysis

© MICROSCOPY SOCIETY OF AMERICA 2012

Single Atom Microscopy

Wu Zhou,[1,2,*] Mark P. Oxley,[1,2] Andrew R. Lupini,[1,2] Ondrej L. Krivanek,[3]
Stephen J. Pennycook,[1,2] and Juan-Carlos Idrobo[1,2,*]

[1]*Materials Science and Technology Division, Oak Ridge National Laboratory, Oak Ridge, TN 37831, USA*
[2]*Department of Physics and Astronomy, Vanderbilt University, Nashville, TN 37235, USA*
[3]*Nion Co., 1102 8th St., Kirkland, WA 98033, USA*

Abstract: We show that aberration-corrected scanning transmission electron microscopy operating at low accelerating voltages is able to analyze, simultaneously and with single atom resolution and sensitivity, the local atomic configuration, chemical identities, and optical response at point defect sites in monolayer graphene. Sequential fast-scan annular dark-field (ADF) imaging provides direct visualization of point defect diffusion within the graphene lattice, with all atoms clearly resolved and identified via quantitative image analysis. Summing multiple ADF frames of stationary defects produce images with minimized statistical noise and reduced distortions of atomic positions. Electron energy-loss spectrum imaging of single atoms allows the delocalization of inelastic scattering to be quantified, and full quantum mechanical calculations are able to describe the delocalization effect with good accuracy. These capabilities open new opportunities to probe the defect structure, defect dynamics, and local optical properties in 2D materials with single atom sensitivity.

Key words: aberration corrected, STEM, ADF imaging, EELS, spectrum imaging, delocalization, plasmons, optical response, single atom, defect, grapheme

Introduction

Being able to see and analyze single atoms, the fundamental building blocks of matter, has been a constant motivation for improving the electron microscope and electron microscopy techniques. The resolution reached by early electron microscopes was orders of magnitude away from visualizing single atoms, but their potential to reach such performance was appreciated from very early on. In 1939, von Ardenne wrote that "sooner or later the ultramicroscopy technique will be able to reveal single atoms and their distribution in the object plane" (von Ardenne, 1939). Early theoretical calculations were also encouraging: based on phase contrast, Schiff estimated that single atoms with atomic number (Z) larger than 7 (i.e., nitrogen) could be imaged at 60 kV (Schiff, 1942).

Reaching such performance in practice required major progress on many fronts, including a substantial improvement in microscope stability, the minimization of lens aberrations, the correction of image astigmatism, and the development of improved electron sources. These advances were realized over about four decades, and in 1970 Crewe et al. were able to obtain the first electron microscope images of single uranium atoms (Crewe et al., 1970). With this step, electron microscopy became the first technique able to image single atoms in "general" samples, rather than on the tip of a sharp conducting needle exposed to an ultrahigh electric field, as had been done in a field ion microscope 14 years earlier (Müller, 1956). Single atom imaging by electron microscopy in turn preceded single atom imaging by scanning tunneling microscopy (Binnig et al., 1983) and related techniques by 13 years.

Received May 25, 2012; accepted August 4, 2012
*Corresponding author. E-mail: wu.zhou@vanderbilt.edu, idrobojc@ornl.gov

Crewe's achievement was made possible by the use of a cold-field emission electron gun in a dedicated scanning transmission electron microscope (STEM) equipped with a high-resolution objective lens, which gave an electron beam of ~5 Å in diameter. Subsequent work by Crewe's group improved the spatial resolution of STEM annular dark-field (ADF) imaging to about 2.5 Å and allowed single atoms as light as silver as well as atomic planes in small crystallites of thorium and uranium to be detected and resolved (Wall et al., 1974). The Crewe group was also able to record movies of atomic motion (Langmore et al., 1974; Isaacson et al., 1977), and they showed that the STEM ADF image intensity of U clusters is proportional to the number of atoms in the cluster, thus demonstrating the incoherent and simple-to-interpret nature of ADF imaging (Retsky, 1974).

To minimize the substrate contrast and variation when imaging single atoms, most of the single atom imaging studies in the 1970s and 1980s made use of ultrathin amorphous carbon films or thin graphite films. Even though the name "graphene" was not used in the TEM context until much later, in retrospect it seems almost certain that (S)TEM images of graphene had actually been obtained already in the 1970s. Isaacson et al. prepared ultrathin (~7 Å average thickness) C films by evaporating high purity graphite onto NaCl and floating the film off in water, and observed discrete quantization of the ADF signal, precisely as if single, double, and thicker layers of graphene were being imaged (Isaacson et al., 1979). It was also shown, in a conventional transmission electron microscope (CTEM), that graphite with W adatoms is thinned by a 100 keV electron beam (Iijima, 1977) to not much thicker than a monolayer. These observations preceded the first electronic

property measurements of graphene (Berger et al., 2004; Novoselov et al., 2004) by more than two decades.

The resolution of the single atom images produced from the 1970s on was almost entirely limited by the spherical aberration of the objective lens, which was minimized by careful design. Further progress only became possible when the aberration was nulled by aberration correction. The need for correction was rigorously demonstrated only a few years after the electron microscope was invented (Scherzer, 1936); solutions for overcoming it were proposed from the 1940s on (Scherzer, 1947; Archard, 1955); and aberration correctors were built from the 1950s on (Seeliger, 1953; Möllenstedt, 1956; Deltrap, 1964). However, the performance of the early aberration correctors was limited by instabilities and parasitic aberrations, and it was only in the late 1990s that the first spherical aberration correctors able to improve the actual resolution of a CTEM (Haider et al., 1998*a*, 1998*b*) and of a STEM (Krivanek et al., 1997, 1999; Batson et al., 2002) were successfully constructed.

With aberration correction, atomic resolution has become routinely attainable at accelerating voltages as low as 60 kV (Krivanek et al., 2010*a*, 2010*b*; Varela et al., 2011), and resolution of 0.5 Å has been demonstrated at 300 kV (Erni et al., 2009). The sensitivity of single atom imaging in the STEM mode has also been significantly improved: single atoms as light as B ($Z = 5$) can now be imaged with medium angle ADF (MAADF) imaging, and the chemical nature of all nonoverlapping atoms in two-dimensional (2D) materials can be identified via quantitative image analysis (Krivanek et al., 2010*a*).

Imaging low-Z 2D materials has thus joined many other applications in which aberration-corrected STEM has been able to demonstrate its power and versatility, such as imaging of single atoms in semiconductors (Lupini & Pennycook, 2003; Allen et al., 2008; Oh et al., 2008), imaging catalysts (Wang et al., 2004; Herzing et al., 2008; Zhou et al., 2009; Ortalan et al., 2010), and three-dimensional (3D) imaging using the reduced depth of focus in aberration-corrected STEM images (van Benthem et al., 2005; Borisevich et al., 2006).

An important benefit of aberration correction is that a high electron current can be packed into an atom-sized probe, which allows signals with weaker cross sections, such as those used by electron energy-loss spectroscopy (EELS) and energy-dispersive X-ray spectroscopy (EDXS), to be collected with atomic resolution and sensitivity. As a consequence, several further advances have been made possible, such as detecting a single impurity atom within a bulk crystal using EELS (Varela et al., 2004), rapid EELS mapping of atomic columns in a complex crystal (Muller et al., 2008), EELS mapping of single atoms (Suenaga et al., 2009) with better spatial resolution than without aberration correction (Suenaga et al., 2000), and EELS fine structure analysis of a graphene edge, which has demonstrated that the edge C atoms are bonded differently than atoms in regular graphene (Suenaga & Koshino, 2010). Optical properties of 2D materials have been analyzed at the atomic scale using valence electron energy-loss (VEEL) spectrum imaging (Zhou et al., 2012*a*), resulting in plasmon maps of monolayer graphene that show sub-nm localized enhancement at a point defect (a Si substitutional atom). The detection of single atoms of Si and Pt using EDXS has also been demonstrated recently (Lovejoy et al., 2012). Further details on the historical development and recent achievements of STEM imaging/spectroscopy and of aberration correction can be found in recent book chapters (Krivanek et al., 2008*b*; Crewe, 2009; Pennycook, 2011).

In this article, we show several examples of imaging and spectroscopy of single atoms, and we illustrate how the experimental results lead to an improved understanding of defects in 2D materials.

Materials and Methods

The graphene sample, obtained from Graphene Supermarket (Reading, MA, USA), was grown on a Ni film on a silicon wafer using the chemical vapor deposition method. Si was found to be a common impurity in this sample, probably due to the use of the silicon wafer. The TEM sample contained both monolayer and multilayer graphene, supported on a 2000-mesh copper grid.

Aberration-corrected STEM imaging and EEL spectrum-imaging experiments were performed with a Nion UltraSTEM100 (Nion Company, Kirkland, WA) (Krivanek et al., 2008*a*), equipped with a cold-field emission electron source and a corrector of third- and fifth-order aberrations. The microscope was operated at 60 kV accelerating voltage, which is below the knock-on radiation damage threshold in graphene. EEL spectra were collected using a Gatan Enfina spectrometer (Gatan, Inc., Pleasanton, CA, USA), with an energy resolution of 0.4 eV at 0.05 eV/channel energy dispersion. For the results shown in this study, the convergence semiangle of the incident probe was set to ~30 mrad, and the EELS collection semiangle to ~48 mrad. MAADF images were collected from ~54 to 200 mrad half-angle range, whereas high-angle ADF (HAADF) images were collected from ~86 to 200 mrad half-angle range.

Sequential images were acquired using a script, written in Gatan's DigitalMicrograph scripting language, which controlled the Nion SuperScan digital acquisition software and hardware. Through the use of buffered acquisition, it was possible to record sequences without introducing delays between frames. The images were aligned prior to their addition by cross correlations with a reference frame selected from the sequence.

STEM-ADF image simulation was performed using the QSTEM simulation package (Koch, 2002). Chromatic and geometric aberrations up to the fifth-order were included in the simulation, using aberration coefficients measured just prior to the experiment. The computed ADF images from QSTEM simulation were convolved with a model of the source to account for the finite source size. Further details of the ADF simulation are discussed with the results.

The simulation of the Si L-shell spectrum image was calculated by convolving the simulated STEM probe with the inelastic scattering potential for Si L-shell ionization (Allen & Josefsson, 1995). Fourier components of the scattering potential were calculated using Hartree Fock wave functions for the bound states and Hartree Slater wave functions for the continuum states (Oxley & Allen, 1998). A collection semiangle of 48 mrad was used, and the result integrated over a 40 eV energy window above threshold. The calculations took into account the geometric and chromatic aberrations, but not the source size. The resultant image was further convolved with a 0.82 Å Gaussian to account for the finite source size.

Results and Discussions

Single Atom Imaging

With the development of aberration-corrected electron microscopes, spherical aberration is no longer the dominant factor that limits the spatial resolution and sensitivity of STEM. The present-day limits on the performance of aberration-corrected STEM as well as technical details on optimizing the microscope for low accelerating voltage applications have been discussed previously (Krivanek et al., 2008*a*, 2010*b*, 2013).

Figure 1 shows an electron probe simulated for our experimental condition (geometric aberration coefficients as measured by auto-tuning, chromatic aberration coefficient of 1.3 mm, and energy spread of 0.35 eV), without considering the finite source size. The chromatic aberration gives a limit on the probe size full-width at half-maximum (FWHM) of about $d_{chrom} = 0.5(\lambda C_c \delta E/E)^{0.5} = 0.96$ Å. In our experiments, the fourth- and fifth-order geometric aberrations were carefully tuned, and the lower order aberrations were adjusted to compensate the residual higher order aberrations. The FWHM of the simulated probe with zero probe current is then about 1 Å (Fig. 1), indicating that the probe size is C_c limited in this case.

For a nonzero probe current, the finite source size also needs to be considered. The size of the electron source projected onto the sample depends on the probe current and the brightness of the electron source as (Krivanek et al., 2011)

$$d_{source} = 2(I_p/B_n V_o^*)^{1/2}/(\pi\alpha),$$

where I_p is the probe current, B_n is the normalized brightness, V_o^* is the relativistically corrected accelerating voltage $V_o^* = V_o(1 + eV_o/2m_e c^2)$, where V_o is the accelerating voltage, m_e is the electron mass, and α is the convergence semiangle. Using a normalized brightness $B_n = 1 \times 10^8$ A/(m^2 sr V) and a probe current of $I_p = 100$ pA, the calculated source size is 0.84 Å, which increases the probe size for nonzero probe current as

$$d_{probe} = (d_{chrom}^2 + d_{source}^2)^{0.5}.$$

Under our experimental conditions, the Nion UltraSTEM provides an electron probe of about 1.3 Å with 100 pA probe current. This probe size is sufficient to resolve the C-C nearest neighbors in graphene, separated by 1.42 Å. This is demonstrated in Figure 2, where individual carbon atoms in the graphene layer are clearly resolved, and information transfer up to 1.065 Å is obtained in the image Fourier transform (FT). The probe current we use is considerably higher than that typically used for high-resolution STEM imaging in a Schottky STEM (10–30 pA). However, as will be discussed later, the high probe current is very useful for performing quantitative STEM image analysis and single atom spectroscopy of light elements.

Figure 3 shows MAADF images of a point defect in monolayer graphene acquired using different dwell times with a 100 pA probe current. The point defect consists of a single Si atom [as identified by quantitative image analysis (Figs. 3, 4) and EELS (Fig. 7)] that replaced two carbon atoms in the graphene lattice and thereby formed two adjacent fivefold rings. Images of the same area were acquired in two different ways: a single scan with a dwell time of 40 μs/pixel (Fig. 3A), and sequential scans with a dwell time of 24 μs/pixel. The sequentially scanned images were aligned by cross-correlation and cropped to show identical sample areas. A sum of 16 aligned images, with a total acquisition time of 384 μs/pixel, is shown in Figure 3C, while a single frame image is shown in Figure 3B. No other processing was applied to the images.

The individual carbon atoms and the Si atom can be clearly resolved in all three images, but one can readily notice that the three images have different quality. Specifically, the signal-to-noise (S/N) ratios, which are related to the electron dose applied to the sample, are substantially different. All three images were acquired with the same 100 pA electron probe and 0.039 Å pixel size. The electron dose was therefore 1.64×10^7 electrons/Å^2 for image 3A, 9.9×10^6 electrons/Å^2 for the single frame image 3B, and 1.58×10^8 electrons/Å^2 for the summed image 3C.

The ADF image signal generated by each carbon atom is given by the product of the electron dose per Å^2 times the scattering cross section. The MAADF cross section for a single C atom imaged at 60 keV with a detector starting at 54 mrad is 1.4×10^{-3} Å^2 (Treacy, 2011). Assuming a MAADF detector with a detective quantum efficiency of 1, the number of electrons counted by the detector per C atom should therefore have been $N \sim 2.3 \times 10^4$ electrons per carbon atom for Figure 3A, 1.4×10^4 electrons per carbon atom for Figure 3B, and 2.2×10^5 electrons per carbon atom in the summed image (Fig. 3C). The root mean square (rms) statistical variation in the signal collected from each carbon atom ($\sqrt{N}$ shot noise) should therefore amount to 0.7%, 0.9%, and 0.2% for Figures 3A, 3B, and 3C, respectively, and the peak-to-peak shot noise should have been about 3.3%, 4.3%, and 1.1%, respectively, when the integrated intensity from each carbon atom is plotted. This is much less than the difference between the total MAADF intensity of atoms differing by $\Delta Z = \pm 1$ from C, i.e., B or N, whose substitution into the graphene lattice produces

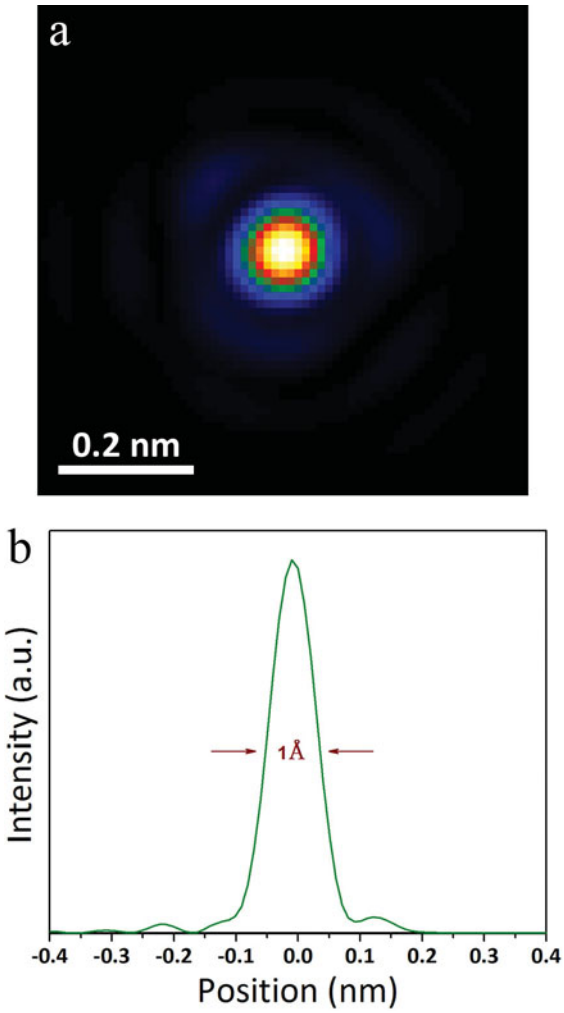

Figure 1. Simulated electron probe, using the chromatic and geometric aberration coefficients measured independently (by EELS and auto-tuning). **a:** Two-dimensional probe intensity distribution. **b:** Intensity profile along the horizontal section of the probe. The FWHM is ~1 Å. The source size was not taken into account in this simulation.

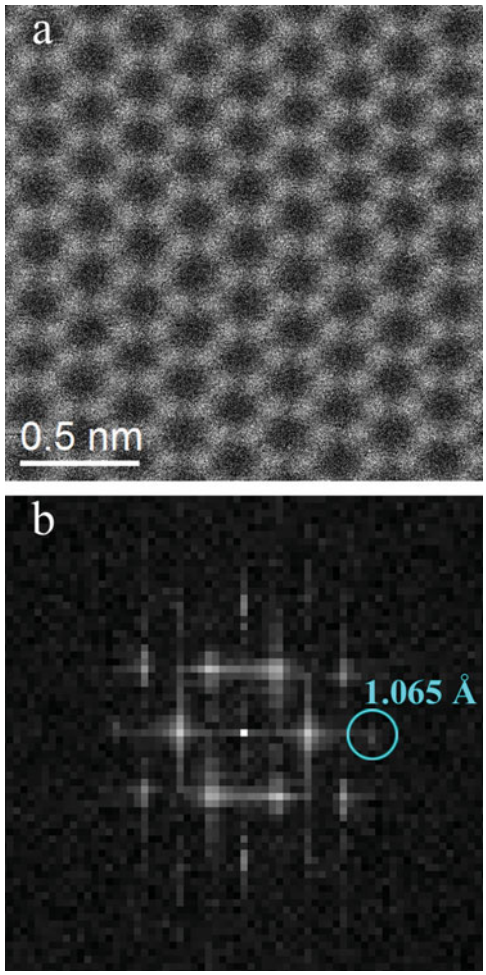

Figure 2. A typical unprocessed MAADF image of (**a**) monolayer graphene and (**b**) the corresponding FT pattern showing information transfer limit of 1.065 Å. The spatial resolution is sufficient to resolve the C-C dumbbells.

about 30% change in the signal per atom (Krivanek et al., 2010*a*). Therefore, in high-dose images such as the ones shown here, quantitative image analysis can be used to chemically identify every atom.

At the single-pixel level, the signal from individual atoms is much weaker: approximately 26, 16, and 254 electrons per pixel, respectively, for the three MAADF images in Figure 3. The rms statistical variation at the single-pixel level should, therefore, amount to 20%, 25%, and 6.2% of the peak intensity from the carbon atoms, respectively. This noise level is roughly what we see directly from the images. Figure 3E shows the intensity line profiles taken along the highlighted trajectories in the MAADF images, integrated over 13 pixels (i.e., 0.5 Å) in the perpendicular direction of the line profiles. The integration reduces the statistical variation in the intensity line profiles by a factor of $13^{1/2}$, to 5.4%, 6.9%, and 1.7% rms for Figures 3A, 3B, and 3C, respectively. The weak per-pixel signal is due to spreading the signal from each atom among many more pixels than the minimum necessary: 3.9 pm pixels were used to sample a ~100 pm resolution image. Provided that doing many digitizations per each atomic image does not inject major read-out noise into the images, such oversampling is however useful. It allows individual atoms to be located with greater precision than in more coarsely sampled images, and it also allows dynamic events such as the atoms jumping away to be observed at μs-level time resolution (Krivanek et al., 2010*b*).

As pointed out previously, quantitative analysis of the image intensity of an atom has to take into account the contribution from its nearest neighbors arising due to the probe tails, which are surprisingly strong in ADF imaging of graphene: up to about 10% of the intensity that belongs in the image of a particular atom can be diverted into the image of its nearest neighbors (Krivanek et al., 2010*a*). This means that up to about 30% of the intensity of each atomic image in graphene can actually be due to the contributions from the atom's three nearest neighbors, and more if any of the neighbors is a heavier dopant. Account-

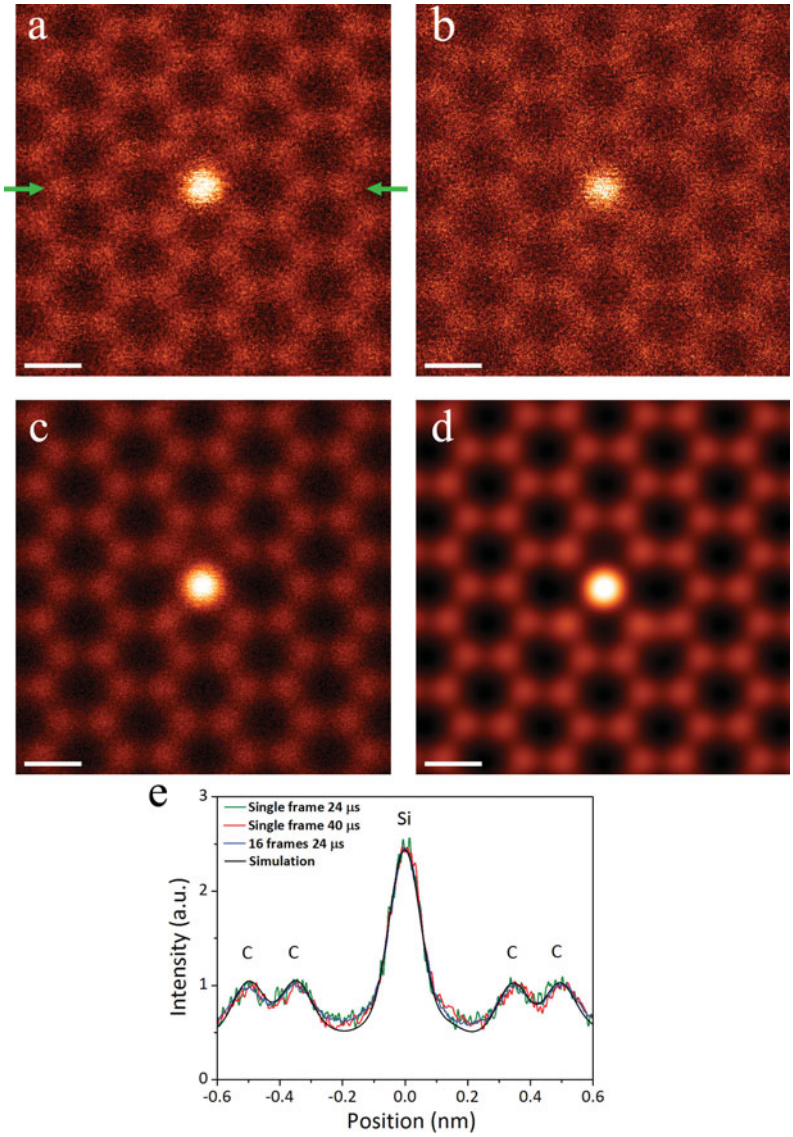

Figure 3. Comparison of S/N ratio for MAADF images acquired using different procedures. (**a**) Single scan with 40 μs/pixel acquisition time; (**b**) single scan with 24 μs/pixel acquisition time; (**c**) stacking of 16 sequential fast-scan images with 24 μs/pixel acquisition time. (**d**) Simulated MAADF image. (**e**) Comparison of intensity line profiles (integration width: 13 pixels) from the three experimental images and the simulated image. Scale bars: 0.2 nm.

ing for this contribution can be done in two different ways: we can perform quantitative image simulation, with the contributions of probe tails included, to match the experimental image; or we can subtract the contribution of the probe tails before analyzing the image.

The quantitative image simulation method is illustrated in Figure 3D. Here, a MAADF image of the point defect was first computed using the QSTEM simulation package (Koch, 2002). The simulation took into account the effect of chromatic and geometric aberrations, determined experimentally, but with a zero source size. The simulated image was further convolved with an artificial probe with FWHM of 0.8 Å, to account for the effect of finite electron source size. By placing a single Si atom substitutionally into the graphene layer at the defect site, the final calculated image (Fig. 3D) provides a good match with the experimental images at all atomic positions (Fig. 3E). The intensity at the center of the hexagonal rings of the graphene lattice is a few percent lower in the calculated image as compared with the experimental images. The discrepancy results from an imperfect modeling of the electron probe tail in the image simulation. Even with this discrepancy, quantitative image simulation provides a feasible way to identify the chemical nature atom-by-atom via ADF imaging without any image processing, which sometimes would induce artifacts. Similar simulations were also able to match an experimental image of a substitutional Si-N pair in the graphene lattice (Zhou et al., 2012*a*).

The second method uses Fourier filtering with a smoothing and tail-subtracting filter (Krivanek et al., 2010*a*, 2013). The filtering, as illustrated by the two "de-tailed" images in Figure 4, reduces the statistical noise in the images and strips off the image contribution due to the tail of the electron probe. In particular, the intensity at the center of the carbon hexagonal rings decreases from ~60% of the intensity of carbon maxima in the raw images to only a few percent (Fig. 4E), and the signals from each atom are now distributed within a peak that is well approximated by a Gaussian with FWHM of ~1.1 Å. A Gaussian of this width decays to 1.0% of its maximum at 1.42 Å away from the

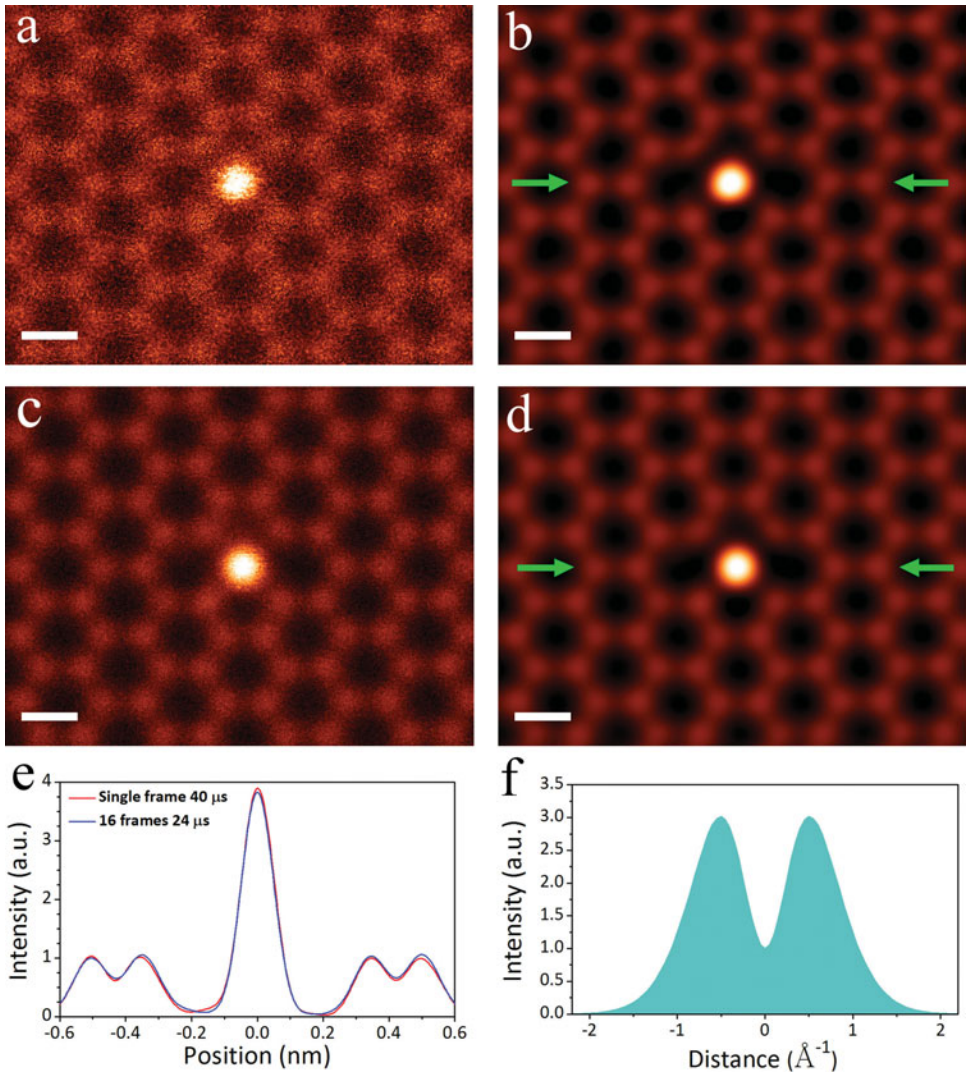

Figure 4. MAADF image contrast analysis via Fourier filtering. (**a**) MAADF image (raw data) taken with 40 μs/pixel acquisition time; (**c**) sum of 16 sequential MAADF images (raw data) taken with 24 μs/pixel acquisition time for each frame; (**b**, **d**) images **a** and **c** processed with a smoothing and probe skirt-removing filter; (**e**) intensity line profiles taken between the two green arrows in the filtered images **b** and **d**; (**f**) the smoothing and skirt-subtracting filter as it was used in the reciprocal space. Scale bars: 0.2 nm.

center, making the contribution to the image intensity of an individual atom from its nearest neighbors practically negligible.

In the example shown in Figure 4, the intensity ratio for the Si and C atoms is 3.9 in the "de-tailed" images. Since $3.9 = (14/6)^{1.61}$, when modeling the MAADF imaging of different Z atoms by a simple power law of the form $I_{Z1}/I_{Z2} = (Z_1/Z_2)^{\exp}$ (Krivanek et al., 2010*a*), the exponent *exp* is thus 1.61. The small deviation of the exponent from the previously reported value of 1.64 most likely arises due to small differences in the ADF detector collection angles, energy spreading, dark level subtraction, imperfect removal of the probe tail, and statistical noise. Had the exponent been 1.64 as in the previous study, the Si/C ratio would have been 4.0. Had the impurity atom been Al ($Z = 13$) or P ($Z = 15$) instead, the ratio would have been 3.5 or 4.4, respectively. This means that even with a small variation in the exact exponent value, the "de-tailed" image allows a Si atom to be distinguished from Al or P, and C atoms from B or N.

Similar arguments show that Li on graphene would generate about 32% of the MAADF image intensity of a carbon atom, and a stable H atom on graphene would generate about 5.5% of the image intensity of a carbon atom. If single Li or H atoms are located in a stable position on graphene and do not move around under high electron dose, they would be detectable by MAADF imaging given that the noise level in the image is much lower than the signals from these single atoms. Fast sequential scans with cross-correlation alignment, as used for Figure 3C, would then be an excellent approach to image stable ultralight adatoms on graphene.

It is useful to note that chemical mapping by quantitative analysis of "de-tailed" ADF images only works well

when all the atoms are clearly separated in the images (Krivanek et al., 2010*a*). When the atoms overlap, e.g., in the case of double-layer graphene or carbon nanotubes, the atomic intensity maxima are not readily separated and assigned to individual atoms, which makes it difficult to quantify the individual intensity of each atom. The presence of heavy elements, such as Au and Pt, can bring extra challenges because it has not yet been experimentally verified that the image intensity follows a simple power law for high-Z atoms too. Moreover, the partially coherent nature of MAADF images can cause the total intensity of two atoms whose projections fall on top of each other to be more than predicted by simple incoherent superposition of the atomic images (Krivanek et al., 2013). However, quantitative image simulation method taking account of partial coherence effects may still be effective in such a situation.

The single-atom images can be used to determine the atomic positions in a complex structure, and it is instructive to estimate the precision with which this can be done. Detailed comparison of the "de-tailed" images in Figures 4B and 4D shows that whereas in the single-scan image of Figure 4B the image maxima of the carbon atoms appear to be randomly shifted by up to about 10 pm from their expected locations defined by the regular graphene lattice, in the multiple-scan image of Figure 4D, the atomic images are located within a few pm (about one pixel) of their expected locations. The statistical error in the location of a 1.3 Å wide maximum arising due to a finite number of electrons contributing to the maximum is $\sim w/(2\sqrt{(N-1)})$, where w is the width of the maximum and N the number of electrons that contributed to it. This amounts to ~0.5 pm for the lower-dose image of Figure 4B and ~0.1 pm for the higher-dose image of Figure 4D. These values cannot explain the observed deviations, whose origin therefore lies in the random "jitter" of the probe relative to the sample, caused by random instabilities in the sample position (mechanical vibrations) and random variations in the probe position due to electrical and magnetic instabilities. In a single-scan image, such deviations are not averaged out, and it is a noteworthy achievement that they do not amount to more than about 10 pm. In the multiple-scan image, they are averaged and are expected to be reduced by about $\sqrt{m}$, where m is the number of scans contributing to an image. In particular, in the 16-image sum of Figures 4C and 4D, the random deviations are reduced by about a factor of 4—a very worthwhile improvement when trying to locate the atomic positions with pm-level precision.

The above discussion shows that recording multiple fast sequential scans is preferable to recording a single slow scan, as long as the individual fast-scan images can provide sufficient S/N level for performing the cross-correlation alignment (Saito et al., 2009). The cross-correlation is performed on the entire image rather than on a single atom; thus, a very high S/N ratio in the individual images is not required. Therefore, an optimum way to acquire STEM images when trying to determine atomic positions with the best precision possible is to acquire more than 100 fast-scan images, which should, in principle, reduce the atomic position jitter by more than a factor of 10. An additional advantage of the multiple scan strategy is that when imaging metastable structures, frames with identical structures can be summed up to improve the S/N ratio (as used in Fig. 3C), while the structural evolution can still be captured in different frames.

Being able to capture structural changes is illustrated in Figure 5. Figures 5A and 5B show frames #16 and #17 of a sequential image dataset, the first 16 frames of which were summed to create Figure 3C. Even though the fourfold coordinated Si defect shown in Figures 3 and 5A was remarkably stable (it remained unchanged over a dose of more than 10^9 electrons used for recording the spectrum image shown in Fig. 7 and the first 16 sequential ADF scans shown in Fig. 4), eventually it transformed into a threefold coordinated Si structure in frame #17, when an additional light atom jumped into the defect site. The additional atom caused the Si atom to move to the right by about 0.7 Å, as can be clearly seen in Figure 5C, in which the frames #16 and #17 are superimposed.

A closer examination of the defect structure in Figure 5B reveals that the "new" additional atom, which is bonded directly with the Si atom, has a slightly higher intensity than carbon (Fig. 6A). Intensity profiles taken along three different directions across the Si atom (Fig. 6C) also show that this "new" atom is brighter than the two C atoms that are bonded directly with the Si atom in the other two equivalent positions. The electron probe used to take these images did not show a significant asymmetric probe tail, as can be seen in Figures 3 and 4. The higher measured intensity therefore indicates that the "new" atom is heavier than C. Quantitative image simulation achieves a good match with the intensity of the experimental image at all the atomic positions when a substitutional N atom is places at the "new" atomic position (Figs. 6B, 6D). Analyzing the image intensity after "de-tailing" leads to the same result.

Monitoring structural changes of a sample is not a new capability for STEM. As mentioned in the Introduction, the diffusion of surface uranium atoms on a thin carbon film had already been studied using STEM ADF imaging many years ago (Langmore et al., 1974; Isaacson et al., 1977). However, those studies could only resolve heavy atoms, and the local chemical environment and bonding of the atoms remained unknown. With aberration correction, we are now able to determine the location and chemical type of every atom present in a monolayer and to follow the motion of single impurity atoms, provided of course that the sample can withstand the high doses necessary for this type of imaging. With further optimization of the image acquisition scheme, a combination of sequential STEM-ADF imaging and theoretical calculations should allow the dynamics of defects to be studied at the single atom level.

Core Loss Spectroscopy of Single Atoms

Elemental analysis using spectroscopic methods, such as EELS or EDXS, provides a specific signal for each atom that

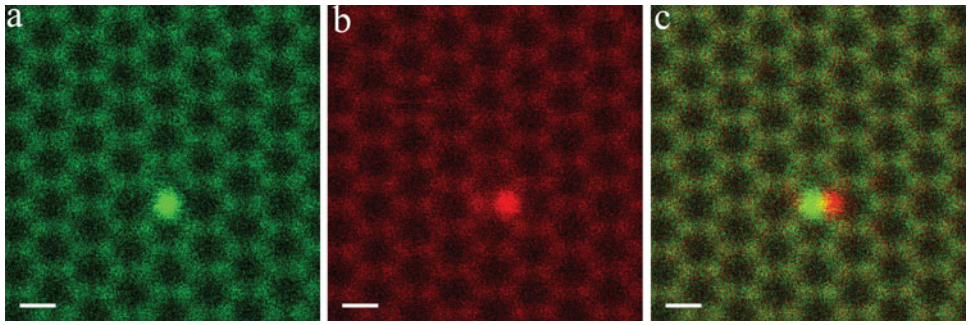

Figure 5. Observation of dynamical structural evolution of point defects in graphene using sequential MAADF imaging. **a:** Frame 16 showing the presence of the same point defect as in Figure 3. **b:** Frame 17 showing the addition of a N atom into the graphene lattice, bonded directly with the substitutional Si atom. **c:** Overlap of images **a** and **b** showing the displacement of the Si atom due to the insertion of the N atom. Scale bars: 0.2 nm.

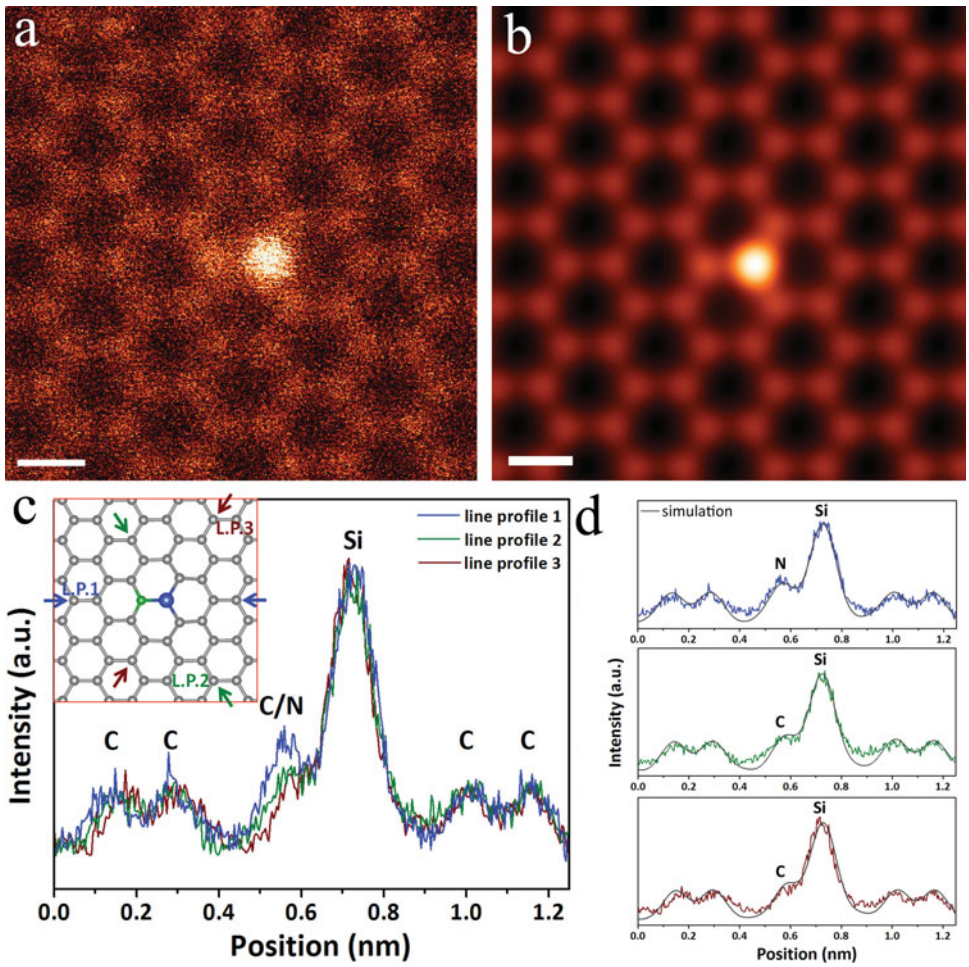

Figure 6. Determination of the structure and chemical identity of individual atoms at a defect site. **a:** Raw experimental MAADF image, cropped from Figure 5b. **b:** Simulated MAADF image. **c:** Comparison of intensity line profiles along different directions from the experimental image. The schematic structural model and the three line profile trajectories are shown as inset. **d:** Comparison of intensity line profiles along different directions from the experimental and simulated images. Color schemes same as in image **c**. Scale bars: 0.2 nm.

is not greatly influenced by its neighbors and is therefore better suited for the case of overlapping atoms. EELS, with its good energy resolution, can also provide additional information on the bonding of the atom, and on the optical response of the material. The advantages of the core-loss spectroscopic methods are somewhat mitigated by the fact that they require much higher electron dose than ADF imaging due to their lower cross sections, and that the spectroscopic signal is typically more delocalized than the ADF one.

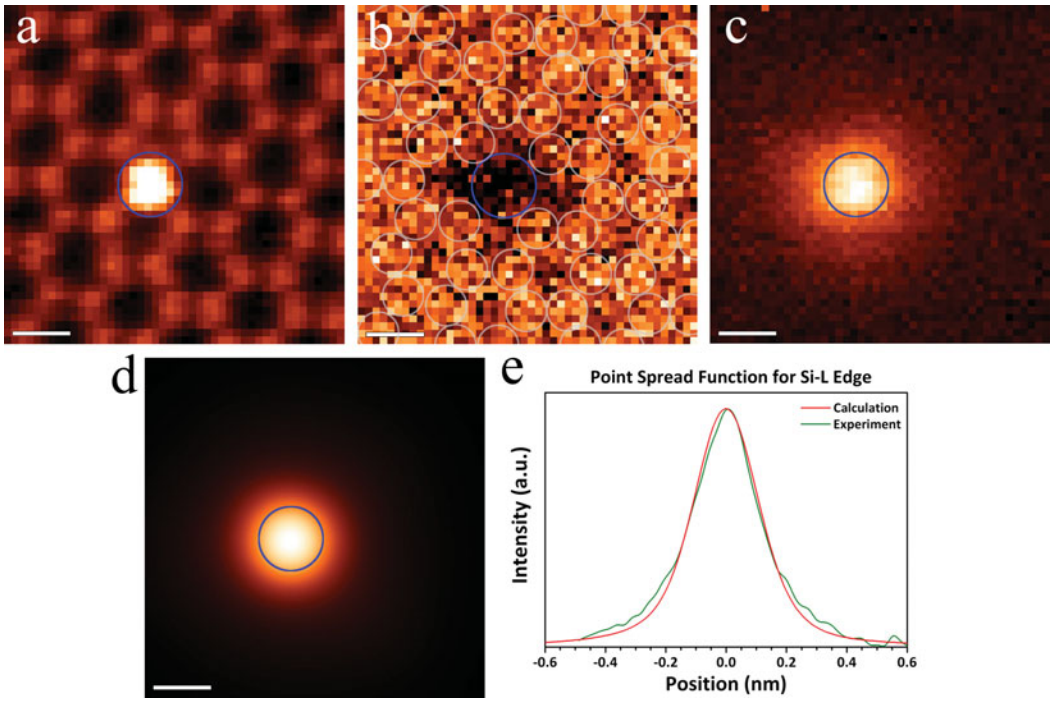

Figure 7. Direct measurement of PSF for Si L-edge from a single substitutional Si atom in monolayer graphene. **a:** HAADF image collected during spectrum imaging. **b:** Carbon K-edge map using an integration energy window of 290–308 eV. The light gray and blue circles highlight the position of the carbon and Si atoms, respectively. **c:** Si L-edge map using an integration energy window of 100–140 eV. The core-loss spectrum images were filtered with PCA and reconstructed with seven principal components. **d:** Calculated 2D Si L-edge distribution from a single Si atom in vacuum. The calculation took into account the geometric and chromatic aberrations. The result was further convolved with a 0.82 Å Gaussian to account for the finite source size. **e:** Comparison of PSF from the experiment and the simulation, measured along the horizontal section of the Si atom. Scale bars: 0.2 nm.

Figure 7 shows STEM-EELS elemental mapping of the substitutional Si defect in monolayer graphene shown in Figures 3 and 4. The spectrum image was acquired with the same 100 pA probe current, with 0.25 Å pixel size and 50 ms/pixel dwell time. EEL spectra were collected with 0.3 eV/channel dispersion and a collection half-angle of 48 mrad. A small pixel size is preferred for high-resolution spectrum imaging, and sample drift should be minimized. However, too-small pixels also need to be avoided, as such pixels are likely to lead to a significant noise increase in the summed EELS signal due to there being many charge-coupled device (CCD) reads, with each one contributing a nonnegligible EELS CCD readout noise term. A pixel size of 0.25 Å, as used here, appears to be a reasonable compromise.

The core-loss range of the spectrum image was filtered using principal component analysis (PCA) (Watanabe, 2011) and reconstructed with seven principal components. PCA filtering helped to reduce the noise level in the experimental measurement, but it is important to note that both the raw data and the PCA filtered data gave the same FWHM value for the point spread function (PSF) in the Si L-edge map.

Figure 7A shows an HAADF image acquired simultaneously with the EEL spectrum image. A slight distortion of the graphene lattice can be noticed in the image, due to the slow scan and a mild sample drift. It should be noted that this specific experimental setup was optimized for low-loss spectrum image (Fig. 8) and delocalization measurement, instead of for elemental mapping. The 100 pA probe current and 0.8 s/Å^2 dwell time gave a dose level (5×10^8 electrons per Å^2) that is relatively low for core-loss mapping. This resulted in a low S/N ratio in the elemental maps, especially in the carbon map (Fig. 7B). Nevertheless, in both the raw data and the PCA-filtered elemental maps, the Si L-edge map clearly shows the presence of a Si atom at the defect core, and the carbon map shows a decrease in the carbon signal due to the two missing carbon atoms. A weak contrast from the hexagonal rings can also be observed in Figure 7B, showing that the carbon map resolution is better than the 2.46 Å ring spacing.

The spatial resolution achievable in an EEL spectrum image is determined by the electron probe size and the delocalization of the inelastic scattering at the actual energy loss. Based on a classical model, delocalization of inelastic scattering can be estimated as (Egerton, 2011)

$$L_{50} \approx 0.5\lambda/\theta_E^{3/4},$$

where L_{50} is the width containing 50% of the total scattered electrons, λ is the electron wavelength, and θ_E is the characteristic EELS scattering angle given by $\theta_E = \Delta E/2E_0$ (ΔE is the energy-loss and E_0 the energy of the incident beam). However, our recent experimental results show that delocalization depends both on the energy loss and the specific

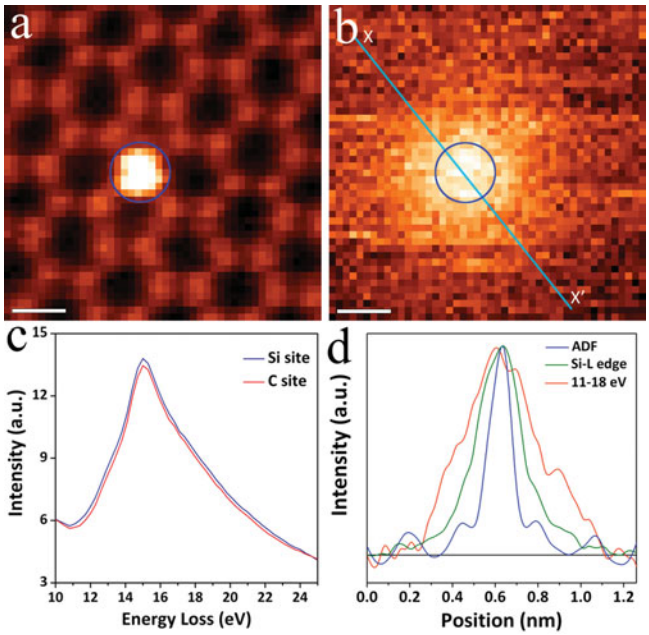

Figure 8. VEEL spectrum image from a single substitutional Si defect in graphene layer showing localized plasmon enhancement. **a:** HAADF image collected during spectrum imaging. **b:** Plasmon map (11–18 eV, *raw data*) showing localized enhancement of the $\pi + \sigma$ plasmon at the Si atom. The blue circle highlights the position of the Si atom. **c:** Comparison of the $\pi + \sigma$ plasmon spectra, extracted from the Si atomic site and from the carbon site. **d:** Comparison of the localization of the HAADF signal, the Si-L edge signal, and the enhanced plasmon intensity from the substitutional Si atom. Line intensity profiles were taken along the line (x-x') indicated in image **b**. Scale bars: 0.2 nm. Images **a**, **b**, and **d** are modified from Zhou et al. (2012*a*) with permission.

electron excitation mode contributing to the energy loss, and in some cases, the experimentally measured delocalization can be considerably smaller than the classical estimate (Zhou et al., 2012*b*). The results highlight the need for quantitative experimental measurement and full quantum mechanical calculations for the delocalization of inelastic electron scattering events.

Figure 7D shows the calculated 2D Si-L edge distribution from a single Si atom in vacuum based on a full quantum mechanical simulation (see the Materials and Methods section). The calculations took into account the geometric and chromatic aberrations. The result was further convolved with a 0.82 Å Gaussian to account for the finite source size. Figure 7E compares the experimental measurement of the PSF for the Si-L edge with the theoretical calculations. The line profiles were taken along the horizontal directions across the Si atom. The experimental FWHM of the Si L-edge PSF is 2.6 Å, which is in excellent agreement with the theoretical calculation. Assuming that the probe size and the intrinsic delocalization are added in quadrature leads to an intrinsic delocalization for the Si-L edge at 100 eV energy loss of about 2.3 Å FWHM. This value is much smaller than the value of 5.0 Å estimated from the classical argument (Egerton, 2011) and is also smaller than the experimental results by Mory et al. (1991) on the attainable spatial resolution of uranium $O_{4,5}$ edge at ~100 eV energy loss.

The results above show that a stationary single atom is an ideal test sample for exploring delocalization quantitatively and also that a full quantum mechanical calculation is needed to fully describe the observed delocalization effect. Stable sites for substitutional N, Fe, and Co atoms in monolayer graphene have been observed in our experiments (Li et al., 2012; Zhou et al., 2012*a*). High-resolution EEL spectrum imaging of these single atoms should provide direct and accurate experimental measurement of delocalization for energy losses spanning from 54 eV (Fe $M_{2,3}$ edge) to 779 eV (Co $L_{2,3}$ edge). The single stationary atoms can also serve as ideal test samples for verifying the accuracy of theoretically predicted scattering cross sections. Moreover, when Si $L_{2,3}$ spectrum images are acquired with electron doses of the order of 10^9 electrons per $Å^2$, near edge fine structures can be observed in the EEL spectra of single Si atoms, providing a direct probe of atomic bonding at the single atom level.

Single Atom Spectroscopy with Valence Electron Excitations

Valence EEL (VEEL) spectroscopy of valence electron excitations is directly related to the dielectric function of the material and provides rich information about the optical and plasmon properties of materials (Erni & Browning, 2005; Browning et al., 2011). VEEL spectrum imaging has been widely applied to map out the surface plasmon response from metallic nanostructures supported on dielectric substrates (Bosman et al., 2007; Nelayah et al., 2007; Guiton et al., 2011; Rossouw et al., 2011). Most of these studies can only achieve sub-10 nm spatial resolution. This is consistent with the common understanding that valence electron excitations, especially plasmons, are highly delocalized. Moreover, in 3D materials, it is almost impossible to define the position and chemical identity of all the atoms, and the effect of a single atom on the valence electron excitation of the whole material can be rather subtle and well below the detection limits of VEELS.

Recently, we have reported experimental evidence that the optical properties of 2D materials can be mapped at the atomic scale using VEEL spectrum imaging (Zhou et al., 2012*a*). The key result is shown in Figure 8. The valence excitation map in Figure 8B was extracted from the same spectrum image dataset as the data of Figure 7, and the EELS intensity was integrated over an energy window between 11 to 18 eV, without background subtraction or filtering of any sort. This energy range covers the major absorption peak at 15.3 eV, commonly referred to as the $\pi + \sigma$ graphene plasmon.

Whereas the $\pi + \sigma$ plasmon map from perfect graphene lattice does not show any localized features, the plasmon map from the point defect (Fig. 8B) shows a local enhancement at the Si atom. The enhancement is not large: the total signal in the 11–18 eV range is increased by less than 3% at the Si atom position. This is illustrated in

Figure 8C, in which the VEEL spectra extracted from the Si position and normal graphene lattice are compared. Intensity over the whole energy range of the $\pi + \sigma$ plasmon (11–24 eV) is enhanced at the Si position, by a small but clearly identifiable amount. The 11–18 eV integration energy window was chosen for the best S/N ratio in the plasmon map shown in Figure 8B.

To map out the small signal change, a high electron dose was needed. With a dose level of 5×10^8 electrons/Å^2, the average intensity in the plasmon map (Fig. 8B) was about 1.8×10^4 electrons/pixel (9×10^4 counts/pixel), giving a pixel-to-pixel noise level of ~0.3% rms. The S/N ratio for the plasmon enhancement effect in the experimental plasmon map, measured at the maximum of the Si position after subtracting the constant background of graphene, is about 7.6. Increasing the dwell time would help to improve the S/N ratio in the mapping, but at the price of more distortion in the spectrum image due to a longer acquisition time.

The localization of the plasmon enhancement effect from the single Si atom is quantified in Figure 8D. The intensity line profile taken from the experimental plasmon map, after subtracting a constant background of graphene, has a FWHM of 4.1 ± 0.3 Å, whereas the HAADF signal has a FWHM of 1.3 Å, and the Si L-edge signal has a FWHM of 2.6 Å. The localization of the plasmon enhancement effect, at the 11–18 eV energy range, is much smaller than the classical estimate (Egerton, 2011), and it is also considerably smaller than the width of the $\pi + \sigma$ plasmon decay measured directly at a graphene edge (Zhou et al., 2012*b*). A localized enhancement at the Si atom was also observed at the absorption peak at ~5 eV, commonly referred to as the π graphene plasmon. This suggests that the localization of a specific inelastic scattering event depends both on the energy loss and the electron excitation mode that contributes to the inelastic scattering. The effect could also be due to enhanced interband transitions at the Si atom that happen to be occurring at the same energy range as the plasmon peaks. Theoretical studies of the highly localized plasmon enhancement effect are now under way.

Conclusion

In his famous 1959 lecture "There's plenty of room at the bottom," Richard Feynman raised the question, "Is there no way to make the electron microscope more powerful?" Based on the diffraction limit of medium energy electrons, he foresaw that the electron microscope could in principle be made 100 times better and that "it should be possible to see the individual atoms." With this, he described a fascinating future for fundamental research in chemistry: "It would be very easy to make an analysis of any complicated chemical substance; all one would have to do would be to look at it and see where the atoms are."

After several decades of continuous development, electron microscopy is now able to match Feynman's prediction in damage-resistant materials. As shown in this article, quantitative ADF imaging and EEL spectrum imaging in an aberration-corrected STEM are now capable of atom-by-atom chemical analysis, for atoms as light as C and probably even lighter. ADF imaging can track atoms diffusing in the graphene lattice and provide full description of their local chemical environment. These are important steps toward the visualization of molecular dynamics at atomic resolution. Using fast sequential image acquisition, positions for damage-resistant atoms can be measured in the STEM with a precision of a few pm, and probably better than 1 pm in the future. With aberration-corrected STEM, delocalization of inelastic scattering of atoms can be directly quantified, and the contribution of single dopant atoms to the local optical properties of materials can be measured.

In summary, imaging and spectroscopy by aberration-corrected STEM offer fundamentally new opportunities to address basic questions in chemistry, physics, and material science at the single atom level. Richard Feynman would have been happy to see this progress.

Acknowledgments

This research was supported by National Science Foundation grant No. DMR-0938330 (W.Z., M.P.O.); Oak Ridge National Laboratory's Shared Research Equipment (ShaRE) User Program (J.C.I.), which is sponsored by the Office of Basic Energy Sciences, U.S. Department of Energy; and the Office of Basic Energy Sciences, Materials Sciences and Engineering Division, U.S. Department of Energy (A.R.L., S.J.P.).

References

Allen, J.E., Hemesath, E.R., Perea, D.E., Lensch-Falk, J.L., Li, Z.Y., Yin, F., Gass, M.H., Wang, P., Bleloch, A.L., Palmer, R.E. & Lauhon, L.J. (2008). High-resolution detection of Au catalyst atoms in Si nanowires. *Nat Nanotechnol* **3**, 168–173.

Allen, L.J. & Josefsson, T.J. (1995). Inelastic scattering of fast electrons by crystals. *Phys Rev B* **52**, 3184–3196.

Archard, G.D. (1955). Two new simplified systems for the correction of spherical aberration in electron lenses. *Proc Phys Soc B* **68**, 156–164.

Batson, P.E., Dellby, N. & Krivanek, O.L. (2002). Sub-angstrom resolution using aberration corrected electron optics. *Nature* **418**, 617–620.

Berger, C., Song, Z.M., Li, T.B., Li, X.B., Ogbazghi, A.Y., Feng, R., Dai, Z.T., Marchenkov, A.N., Conrad, E.H., First, P.N. & de Heer, W.A. (2004). Ultrathin epitaxial graphite: 2D electron gas properties and a route toward graphene-based nanoelectronics. *J Phys Chem B* **108**, 19912–19916.

Binnig, G., Rohrer, H., Gerber, C. & Weibel, E. (1983). 7 × 7 Reconstruction on Si(111) resolved in real space. *Phys Rev Lett* **50**, 120–123.

Borisevich, A.Y., Lupini, A.R. & Pennycook, S.J. (2006). Depth sectioning with the aberration-corrected scanning transmission electron microscope. *Proc Natl Acad Sci USA* **103**, 3044–3048.

Bosman, M., Keast, V.J., Watanabe, M., Maaroof, A.I. & Cortie, M.B. (2007). Mapping surface plasmons at the nanometre scale with an electron beam. *Nanotechnology* **18**, 165505.

Browning, N.D., Arslan, I., Erni, R. & Reed, B.W. (2011). Low-loss EELS in the STEM. In *Scanning Transmission Electron*

Microscopy: Imaging and Analysis, Pennycook, S.J. & Nellist, P.D. (Eds.), pp. 659–688. New York: Springer.

Crewe, A.V. (2009). The work of Albert Victor Crewe on the scanning transmission electron microscope and related topics. In *Advances in Imaging and Electron Physics: Cold Field Emission and the Scanning Transmission Electron Microscope*, Hawkes, P.W. (Ed.), pp. 1–61. San Diego, CA: Academic Press.

Crewe, A.V., Wall, J. & Langmore, J. (1970). Visibility of single atoms. *Science* **168**, 1338–1340.

Deltrap, J.H.M. (1964). Correction of spherical aberration with combined quadrupole-octopole units. *3rd European Conference on Electron Microscopy*, Prague, Czech Republic, pp. 45–46. Czechoslovak Academy of Sciences.

Egerton, R.F. (2011). *Electron Energy-Loss Spectroscopy in the Electron Microscopy*. New York: Springer.

Erni, R. & Browning, N.D. (2005). Valence electron energy-loss spectroscopy in monochromated scanning transmission electron microscopy. *Ultramicroscopy* **104**, 176–192.

Erni, R., Rossell, M.D., Kisielowski, C. & Dahmen, U. (2009). Atomic-resolution imaging with a sub-50-pm electron probe. *Phys Rev Lett* **102**, 096101.

Guiton, B.S., Iberi, V., Li, S., Leonard, D.N., Parish, C.M., Kotula, P.G., Varela, M., Schatz, G.C., Pennycook, S.J. & Camden, J.P. (2011). Correlated optical measurements and plasmon mapping of silver nanorods. *Nano Lett* **11**, 3482–3488.

Haider, M., Rose, H., Uhlemann, S., Schwan, E., Kabius, B. & Urban, K. (1998*a*). A spherical-aberration-corrected 200 kV transmission electron microscope. *Ultramicroscopy* **75**, 53–60.

Haider, M., Uhlemann, S., Schwan, E., Rose, H., Kabius, B. & Urban, K. (1998*b*). Electron microscopy image enhanced. *Nature* **392**, 768–769.

Herzing, A.A., Kiely, C.J., Carley, A.F., Landon, P. & Hutchings, G.J. (2008). Identification of active gold nanoclusters on iron oxide supports for CO oxidation. *Science* **321**, 1331–1335.

Iijima, S. (1977). Observation of single and clusters of atoms in bright field electron-microscopy. *Optik* **48**, 193–214.

Isaacson, M., Kopf, D., Utlaut, M., Parker, N.W. & Crewe, A.V. (1977). Direct observations of atomic diffusion by scanning transmission electron microscopy. *Proc Natl Acad Sci USA* **74**, 1802–1806.

Isaacson, M., Ohtsuki, M. & Utlaut, M. (1979). Can we determine the structure of thin amorphous film using scanning transmission electron microscopy? *Proceeding of the 37th Annual EMSA Meeting*, San Antonio, TX, pp. 498–501. Electron Microscopy Society of America.

Koch, C.T. (2002). Determination of core structure periodicity and point defect density along dislocations. PhD Thesis. Pheonix, AZ: Arizona State University.

Krivanek, O.L., Chisholm, M.F., Dellby, N. & Murfitt, M.E. (2011). Atomic-resolution STEM at low primary energies. In *Scanning Transmission Electron Microsocpy: Imaging and Analysis*, Pennycook, S.J. & Nellist, P.D. (Eds.), pp. 615–658. New York: Springer.

Krivanek, O.L., Chisholm, M.F., Nicolosi, V., Pennycook, T.J., Corbin, G.J., Dellby, N., Murfitt, M.F., Own, C.S., Szilagyi, Z.S., Oxley, M.P., Pantelides, S.T. & Pennycook, S.J. (2010*a*). Atom-by-atom structural and chemical analysis by annular dark-field electron microscopy. *Nature* **464**, 571–574.

Krivanek, O.L., Corbin, G.J., Dellby, N., Elston, B.F., Keyse, R.J., Murfitt, M.F., Own, C.S., Szilagyi, Z.S. & Woodruff, J.W. (2008*a*). An electron microscope for the aberration-corrected era. *Ultramicroscopy* **108**, 179–195.

Krivanek, O.L., Dellby, N. & Lupini, A.R. (1999). Towards sub-angstrom electron beams. *Ultramicroscopy* **78**, 1–11.

Krivanek, O.L., Dellby, N. & Murfitt, M.F. (2008*b*). Aberration correction in electron microscopy. In *Handbook of Charged Particle Optics*, Orloff, J. (Eds.), pp. 601–640. Boca Raton, FL: CRC Press.

Krivanek, O.L., Dellby, N., Murfitt, M.F., Chrisholm, M.F., Pennycook, T.J., Suenaga, K. & Nicolosi, V. (2010*b*). Gentle STEM: ADF imaging and EELS at low primary energies. *Ultramicroscopy* **110**, 935–945.

Krivanek, O.L., Dellby, N., Spence, A.J., Camps, R.A. & Brown, L.M. (1997). Aberration correction in the STEM. *IoP Conference Series No. 153*, pp. 35–40. Institute of Physics.

Krivanek, O.L., Zhou, W., Chisholm, M.F., Dellby, N., Lovejoy, T.C., Ramasse, Q.M. & Idrobo, J.C. (2013). Gentle STEM of single atoms: Low keV imaging and analysis at ultimate detection limits. In *Low Voltage Electron Microscopy: Principles and Applications*, Bell, D. & Erdman, N. (Eds.), pp. 119–161. London: John Wiley & Sons.

Langmore, J.P., Isaacson, M.S. & Crewe, A.V. (1974). The study of single heavy atom motion in the STEM. *Proceeding of the 32nd Annual EMSA Meeting*, St. Louis, MO, pp. 378–379. Electron Microscopy Society of America.

Li, Y., Zhou, W., Wang, H., Xie, L., Liang, Y., Wei, F., Idrobo, J.C., Pennycook, S.J. & Dai, H. (2012). An oxygen reduction electrocatalyst based on carbon nanotube-graphene complexes. *Nat Nanotechnol* **7**, 394–400.

Lovejoy, T.C., Ramasse, Q.M., Falke, M., Kaeppel, A., Terborg, R., Zan, R., Dellby, N. & Krivanek, O.L. (2012). Single atom identification by energy dispersive X-ray spectroscopy. *Appl Phys Lett* **100**, 154101.

Lupini, A.R. & Pennycook, S.J. (2003). Localization in elastic and inelastic scattering. *Ultramicroscopy* **96**, 313–322.

Möllenstedt, G. (1956). Elektronenmikroskopische Bilder mit einem nach O. Scherzer sphärisch korrigiertem Objektiv. *Optik* **13**, 209–215.

Mory, C., Kohl, H., Tence, M. & Colliex, C. (1991). Experimental investigation of the ultimate EELS spatial resolution. *Ultramicroscopy* **37**, 191–201.

Muller, D.A., Kourkoutis, L.F., Murfitt, M., Song, J.H., Hwang, H.Y., Silcox, J., Dellby, N. & Krivanek, O.L. (2008). Atomic-scale chemical imaging of composition and bonding by aberration-corrected microscopy. *Science* **319**, 1073–1076.

Müller, E.W. (1956). Resolution of the atomic structure of a metal surface by the field ion microscope. *J Appl Phys* **27**, 474–476.

Nelayah, J., Kociak, M., Stephan, O., Garcia de Abajo, F.J., Tence, M., Henrard, L., Taverna, D., Pastoriza-Santos, I., Liz-Marzan, L.M. & Colliex, C. (2007). Mapping surface plasmons on a single metallic nanoparticle. *Nat Phys* **3**, 348–353.

Novoselov, K.S., Geim, A.K., Morozov, S.V., Jiang, D., Zhang, Y., Dubonos, S.V., Grigorieva, I.V. & Firsov, A.A. (2004). Electric field effect in atomically thin carbon films. *Science* **306**, 666–669.

Oh, S.H., van Benthem, K., Molina, S.I., Borisevich, A.Y., Luo, W., Werner, P., Zakharov, N.D., Kurnar, D., Pantelides, S.T. & Pennycook, S.J. (2008). Point defect configurations of supersaturated Au atoms inside Si nanowires. *Nano Lett* **8**, 1016–1019.

Ortalan, V., Uzun, A., Gates, B.C. & Browning, N.D. (2010). Direct imaging of single metal atoms and clusters in the pores of dealuminated HY zeolite. *Nat Nanotechnol* **5**, 506–510.

Oxley, M.P. & Allen, L.J. (1998). Delocalization of the effective interaction for inner-shell ionization in crystals. *Phys Rev B* **57**, 3273–3282.

Pennycook, S.J. (2011). A scan through the history of STEM. In *Scanning Transmission Electron Microscopy: Imaging and Analysis*, Pennycook, S.J. & Nellist, P.D. (Eds.), pp. 1–90. New York: Springer.

Retsky, M. (1974). Observed single atom elastic cross-sections in a scanning electron-microscope. *Optik* **41**, 127–142.

Rossouw, D., Couillard, M., Vickery, J., Kumacheva, E. & Botton, G.A. (2011). Multipolar plasmonic resonances in silver nanowire antennas imaged with a subnanometer electron probe. *Nano Lett* **11**, 1499–1504.

Saito, M., Kimoto, K., Nagai, T., Fukushima, S., Akahoshi, D., Kuwahara, H., Matsui, Y. & Ishizuka, K. (2009). Local crystal structure analysis with 10-pm accuracy using scanning transmission electron microscopy. *J Electron Microsc* **58**, 131–136.

Scherzer, O. (1936). Uber einige Fehler von Elektronenlinsen. *Z Phys* **101**, 114–132.

Scherzer, O. (1947). Sphärische und chromatische Korrektur von Elektronenlinsen. *Optik* **2**, 114–132.

Schiff, L.I. (1942). Ultimate resolving power of the electron microscope. *Phys Rev* **61**, 721–722.

Seeliger, R. (1953). Über die justierung sphärisch korrigierter elektronenoptischer systeme. *Optik* **10**, 29–41.

Suenaga, K. & Koshino, M. (2010). Atom-by-atom spectroscopy at graphene edge. *Nature* **468**, 1088–1090.

Suenaga, K., Sato, Y., Liu, Z., Kataura, H., Okazaki, T., Kimoto, K., Sawada, H., Sasaki, T., Omoto, K., Tomita, T., Kaneyama, T. & Kondo, Y. (2009). Visualizing and identifying single atoms using electron energy-loss spectroscopy with low accelerating voltage. *Nat Chem* **1**, 415–418.

Suenaga, K., Tence, T., Mory, C., Colliex, C., Kato, H., Okazaki, T., Shinohara, H., Hirahara, K., Bandow, S. & Iijima, S. (2000). Element-selective single atom imaging. *Science* **290**, 2280–2282.

Treacy, M.M.J. (2011). Z dependence of electron scattering by single atoms into annular dark-field detectors. *Microsc Microanal* **17**, 847–858.

van Benthem, K., Lupini, A.R., Kim, M., Baik, H.S., Doh, S., Lee, J.H., Oxley, M.P., Findlay, S.D., Allen, L.J., Luck, J.T. & Pennycook, S.J. (2005). Three-dimensional imaging of individual hafnium atoms inside a semiconductor device. *Appl Phys Lett* **87**, 034104.

Varela, M., Findlay, S.D., Lupini, A.R., Christen, H.M., Borisevich, A.Y., Dellby, N., Krivanek, O.L., Nellist, P.D., Oxley, M.P., Allen, L.J. & Pennycook, S.J. (2004). Spectroscopic imaging of single atoms within a bulk solid. *Phys Rev Lett* **92**, 095502.

Varela, M., Gazquez, J., Pennycook, T.J., Magen, C., Oxley, M.P. & Pennycook, S.J. (2011). Applications of aberration-corrected scanning transmission electron microscopy and electron energy loss spectroscopy to complex oxide materials. In *Scanning Transmission Electron Microscopy: Imaging and Analysis*, Pennycook, S.J. & Nellist, P.D. (Eds.), pp. 429–466. New York: Springer.

von Ardenne, M. (1939). Intensitätsfragen und Auflösungsvermögen des Elektronenmikroskops. *Z Phys* **112**, 744–752.

Wall, J., Langmore, J., Isaacson, M. & Crewe, A.V. (1974). Scanning-transmission electron-microscopy at high-resolution. *Proc Natl Acad Sci USA* **71**, 1–5.

Wang, S., Borisevich, A.Y., Rashkeev, S.N., Glazoff, M.V., Sohlberg, K., Pennycook, S.J. & Pantelides, S.T. (2004). Dopants adsorbed as single atoms prevent degradation of catalysts. *Nat Mater* **3**, 143–146.

Watanabe, M. (2011). X-ray energy-dispersive spectrometry in scanning tranmission electron microscopes. In *Scanning Transmission Electron Microscopy: Imaging and Analysis*, Pennycook, S.J. & Nellist, P.D. (Eds.), pp. 291–351. New York: Springer.

Zhou, W., Lee, J., Nanda, J., Pantelides, S.T., Pennycook, S.J. & Idrobo, J.C. (2012*a*). Atomically localized plasmon enhancement in monolayer graphene. *Nat Nanotechnol* **7**, 161–165.

Zhou, W., Pennycook, S.J. & Idrobo, J.C. (2012*b*). Localization of inelastic electron scattering in the low-loss energy regime. *Ultramicroscopy* **119**, 51–56.

Zhou, W., Ross-Medgaarden, E.I., Knowles, W.V., Wong, M.S., Wachs, I.E. & Kiely, C.J. (2009). Identification of active Zr-WO_x clusters on ZrO_2 support for solid acid catalysts. *Nat Chem* **1**, 722–728.